nature communications

Article

https://doi.org/10.1038/s41467-024-52004-2

Stabilized $Cu^{\delta+}$-OH species on in situ reconstructed Cu nanoparticles for CO_2-to-C_2H_4 conversion in neutral media

Received: 10 August 2023

Accepted: 22 August 2024

Published online: 29 August 2024

Check for updates

Lei Wang[1,2,9], Zhiwen Chen[3,9], Yi Xiao[1], Linke Huang[3], Xiyang Wang[1], Holly Fruehwald[4], Dmitry Akhmetzyanov[4,5], Mathew Hanson[1], Zuolong Chen[1,2], Ning Chen[6], Brant Billinghurst[6], Rodney D. L. Smith[2,4], Chandra Veer Singh[3,7] ✉, Zhongchao Tan[1,8] ✉ & Yimin A. Wu[1,2,4] ✉

Achieving large-scale electrochemical CO_2 reduction to multicarbon products with high selectivity using membrane electrode assembly (MEA) electrolyzers in neutral electrolyte is promising for carbon neutrality. However, the unsatisfactory multicarbon products selectivity and unclear reaction mechanisms in an MEA have hindered its further development. Here, we report a strategy that manipulates the interfacial microenvironment of Cu nanoparticles in an MEA to suppress hydrogen evolution reaction and enhance C_2H_4 conversion. In situ multimodal characterizations consistently reveal well-stabilized $Cu^{\delta+}$-OH species as active sites during MEA testing. The OH radicals generated in situ from water create a locally oxidative microenvironment on the copper surface, stabilizing the $Cu^{\delta+}$ species and leading to an irreversible and asynchronous change in morphology and valence, yielding high-curvature nanowhiskers. Consequently, we deliver a selective C_2H_4 production with a Faradaic efficiency of 55.6% ± 2.8 at 316 mA cm^{-2} in neutral media.

Electrochemical CO_2 reduction (eCO_2RR) into value-added chemicals and fuels using renewable energy sources holds great promise for mitigating CO_2 emissions[1,2], but it remains at the exploratory stage. The past few decades have seen significant progress in converting CO_2 to targeted products at a lab scale[3]. However, the transition from lab-scale studies to highly efficient, industrial-scale production of eCO_2RR remains a formidable obstacle. The reactions in an assembled catalyst within an eCO_2RR system (e.g., flow cell or MEA) greatly deviate from the traditional ones obtained in an H-cell, introducing new complexities and dynamics that significantly affect reaction kinetics, product selectivity, and overall performance[4,5]. Therefore, a comprehensive understanding of the mechanisms in CO_2 electrolyzers is urgently needed for the development of industrial eCO_2RR technologies.

Reactor engineering is crucial for the successful implementation of efficient and scalable eCO_2RR. Compared to flow cells, the MEA configuration leverages the gas diffusion electrode (GDE) of a flow cell, minimizing the electrolyte usage by direct contact of the catalyst layer with the ion exchange membrane. As a result, it mitigates cell resistance, boosts energy efficiency, and improves cell stability, making it more feasible for practical applications[6]. However, applying the highly efficient electrocatalysts developed in lab-scale tests in an MEA reactor often leads to significant variations in eCO_2RR performance when employing different electrolytes[5]. Specifically, although a highly

[1]Department of Mechanical and Mechatronics Engineering, University of Waterloo, Waterloo, ON N2L 3G1, Canada. [2]Waterloo Institute for Nanotechnology, University of Waterloo, Waterloo, ON N2L 3G1, Canada. [3]Department of Materials Science and Engineering, University of Toronto, Toronto, ON M5S 3E4, Canada. [4]Department of Chemistry, University of Waterloo, Waterloo, ON N2L 3G1, Canada. [5]Institute for Quantum Computing, University of Waterloo, Waterloo, ON N2L 3G1, Canada. [6]Canadian Light Source, Saskatoon, SK S7N 2V3, Canada. [7]Department of Mechanical and Industrial Engineering, University of Toronto, Toronto, ON M5S 3G8, Canada. [8]Eastern Institute of Technology, No. 568 Tongxin Road, Zhenhai District, Ningbo, Zhejiang 315200, China. [9]These authors contributed equally: Lei Wang, Zhiwen Chen. ✉e-mail: chandraveer.singh@utoronto.ca; tanz@uwaterloo.ca; yimin.wu@uwaterloo.ca

alkaline environment, such as 1 M KOH or higher concentrations, increases the pH value on catalyst surfaces, suppressing the hydrogen evolution reaction (HER) and accelerating the formation of multi-carbon products[7], using strong alkaline electrolytes leads to the low CO_2 utilization efficiency and irreversible acidification of the electrolytes, posing challenges in achieving optimal performance[6,8]. In an acidic environment, such as 0.05 M H_2SO_4 and 2.5 M KCl electrolytes, the typical Faradaic efficiency (FE) of the HER side reaction is 20% or higher, which is energy-intensive and suppresses the eCO_2RR. Additionally, the reactor corrosion in an acidic environment reduces the system's stability[9]. The drawbacks of low CO_2 utilization in alkaline electrolytes and strong HER in acid electrolytes could be significantly alleviated by using neutral electrolytes. However, the product selectivity of eCO_2RR in neutral electrolytes is lower than that in alkaline electrolyte[10,11]. Furthermore, achieving high selectivity for eCO_2RR to C_{2+} products (e.g., ethylene and ethanol) in an MEA reactor at industrially relevant current densities represents a significant scientific and technological challenge, although state-of-the-art electrocatalysts have demonstrated remarkable progress in C_1 products (e.g., CO or HCOOH)[12,13].

Another major obstacle to the practical application of eCO_2RR is the lack of a deep understanding of the fundamentals and mechanisms behind eCO_2RR to C_{2+} multicarbon products in an MEA reactor. Previous studies predominantly focused on catalyst design[14–18], with little attention on the real active sites in Cu-based catalysts. Thus, the real Cu active sites are still debatable due to controversial conclusions in the literature[19–22]. For example, Cu^+, mixed oxidation states ($Cu^{\delta+}$) of Cu (e.g., Cu^{2+}, Cu^+, and Cu^0) or their interface have been identified as the active sites of oxide-derived Cu for promoting CO–CO coupling under eCO_2RR[19,20]. Conversely, another study suggests that metallic Cu is the active site of bulk Cu catalysts, attributing this to the instability of subsurface oxides under negative cathodic potentials[21]. Additionally, the active site of Cu nanoparticles (NPs) is reported to be metallic Cu nanograin, as investigated through the structural dynamics during the life cycle of Cu NPs using liquid cell scanning transmission electron microscopy[22]. However, the electron beam during operando observations may potentially reduce the catalyst and alter the actual active sites. Furthermore, these studies primarily focus on eCO_2RR reactions in H-cells or flow cells. As a result, it remains unclear whether the proposed reaction mechanisms are applicable to MEA systems owing to the distinct differences in reactor configuration and electrode-electrolyte interface. The structural transformation and actual active sites of Cu NPs during eCO_2RR to C_{2+} products are still unrevealed in an MEA reactor at industrial-level current density.

To enhance industrial-scale CO_2-to-C_2H_4 conversion in an MEA reactor, we introduced activated carbon black (ACB) with different functional groups to manipulate the interfacial microenvironment of Cu NPs in the MEA, enhancing CO coverage to inhibit the HER and promote the desired C_{2+} reaction pathway. Using in situ multimodal characterizations, we identified the stabilized $Cu^{\delta+}$-OH species as the active sites under negative potential during eCO_2RR. The in situ-generated, strongly oxidative OH radicals stabilized the oxidized $Cu^{\delta+}$ species, leading to an irreversible and asynchronous change in morphology and valence, yielding high-curvature nanowhiskers during eCO_2RR in an MEA reactor. The well-stabilized $Cu^{\delta+}$-OH species and high-curvature nanowhiskers synergistically enhance C_2H_4 production during eCO_2RR. By understanding this mechanism, we achieved a competitive FE of 55.6% ± 2.8 for C_2H_4 at a current density of 316 mA cm^{-2} using a mixture of fluorinated carbon black and Cu NPs (F–Cu). The mixture of OH-functionalized carbon black and Cu NPs (OH–Cu) attained an FE of 42.1% ± 2.7 for C_2H_4 at a current density of 356.6 mA cm^{-2}. Both FEs and current densities observed with the inclusion of ACB surpass those achieved with Cu NPs only (i.e., 32.9% ± 1.8 C_2H_4 FE at a current density of 100 mA cm^{-2}). Insights from this reaction mechanism bridge the knowledge gap between lab-scale studies and industrial-scale implementation, contributing to the development of sustainable and carbon-neutral industries.

Results

eCO_2RR performance in an MEA reactor

As-prepared samples were employed as cathode electrocatalysts in the 5 cm^2 MEA reactor (Fig. 1a) to evaluate the effects of ACB on eCO_2RR, including product distributions and current densities. The eCO_2RR activity of commercial Cu NPs served as the baseline for comparison with other electrocatalysts (Supplementary Fig. 1). Major products such as H_2, CO, and C_2H_4 were produced on the Cu NPs, with minimal ethanol detected. The maximum FE obtained was 32.9% ± 1.8 for C_2H_4 at ~100 mA cm^{-2} (Supplementary Fig. 1). However, at higher cathodic potentials, the dominant HER suppressed the C_{2+} reaction pathways, thereby limiting the partial current density of C_{2+} products. To tackle this challenge, ACB with different functional groups was introduced to regulate the interfacial microenvironment of Cu NPs in the MEA reactor. Among all the tested catalysts, F–Cu and OH–Cu exhibited high partial current densities of CO at low cell potentials (Supplementary Fig. 2a), directly influencing the subsequent C–C coupling pathway toward C_2H_4. Comparison of the partial current densities of H_2 and C_2H_4 indicated that the increased selectivity resulted from suppression of HER at high cell potentials (Supplementary Fig. 2b vs Supplementary Fig. 2c). Therefore, at −3.7 V, OH–Cu achieved a FE of 42.1% ± 2.7 for C_2H_4 at a current density of 356.6 mA cm^{-2} (Fig. 1b), while the F–Cu sample demonstrated an FE of 55.6% ± 2.8 for C_2H_4 at a current density of 316 mA cm^{-2} (Fig. 1c). These experimental results indicate that introducing ACB is a promising strategy to enhance the eCO_2RR performance and highlight the significant advancements in the eCO_2RR-to-C_2H_4 production, with F–Cu and OH–Cu showing excellent performance compared to most Cu-based electrocatalysts (Supplementary Table 1).

To determine whether the catalyst's activity correlates directly with the electrochemical surface area (ECSA), we compared the double-layer capacitance (C_{dl}) of all samples. Based on the C_{dl} values, we observed that introducing ACB significantly increased the ECSA of the catalysts, thereby enhancing eCO_2RR activity (Supplementary Fig. 3). However, the ECSA of F–Cu was notably lower than that of OH–Cu. The higher activity of F–Cu indicated that ECSA cannot solely determine the enhancement of eCO_2RR activity. The fluorination promoted eCO_2RR activity by a different mechanism, such as water activation. Additionally, we varied the F–CB loading to investigate the effect of the interfacial microenvironment of Cu NPs on eCO_2RR activity (Supplementary Fig. 4). A low-loading F–CB substantially enhanced the intrinsic activity of Cu NPs, as evidenced by a higher C_2H_4 FE (42.5% ± 3.7 at a current density of 269.6 mA cm^{-2}) at −3.6 V (Supplementary Fig. 4a) compared to Cu NPs (Supplementary Fig. 1). However, excessive F–CB loading increased the thickness of the gas diffusion electrode (GDE), thereby hindering the transport of CO_2 to the catalysts surface. Consequently, the increase in C_2H_4 FE (33% ± 4.3) at −3.5 V was lower than that achieved with lower F–CB loading, although the current density (-200 mA cm^{-2}) (Supplementary Fig. 4b) was twice that of Cu NPs at −3.3 V (Supplementary Fig. 1). This indicates that the modulation of the interfacial microenvironment follows a volcano-shaped curve (Supplementary Fig. 4c), necessitating the identification of an optimal loading to effectively enhance the catalyst's performance.

Long-term testing was conducted to assess the stability of the F–Cu catalyst in the 5 cm^2 MEA reactor (Fig. 1d). At a current density of 300 mA cm^{-2}, the catalyst operated continuously for 35 h with C_2H_4 selectivity decreasing only from 50% initially to 42%. This highlights the potential of F–Cu for industrial-relevant eCO_2RR conversion.

https://doi.org/10.1038/s41467-024-52004-2

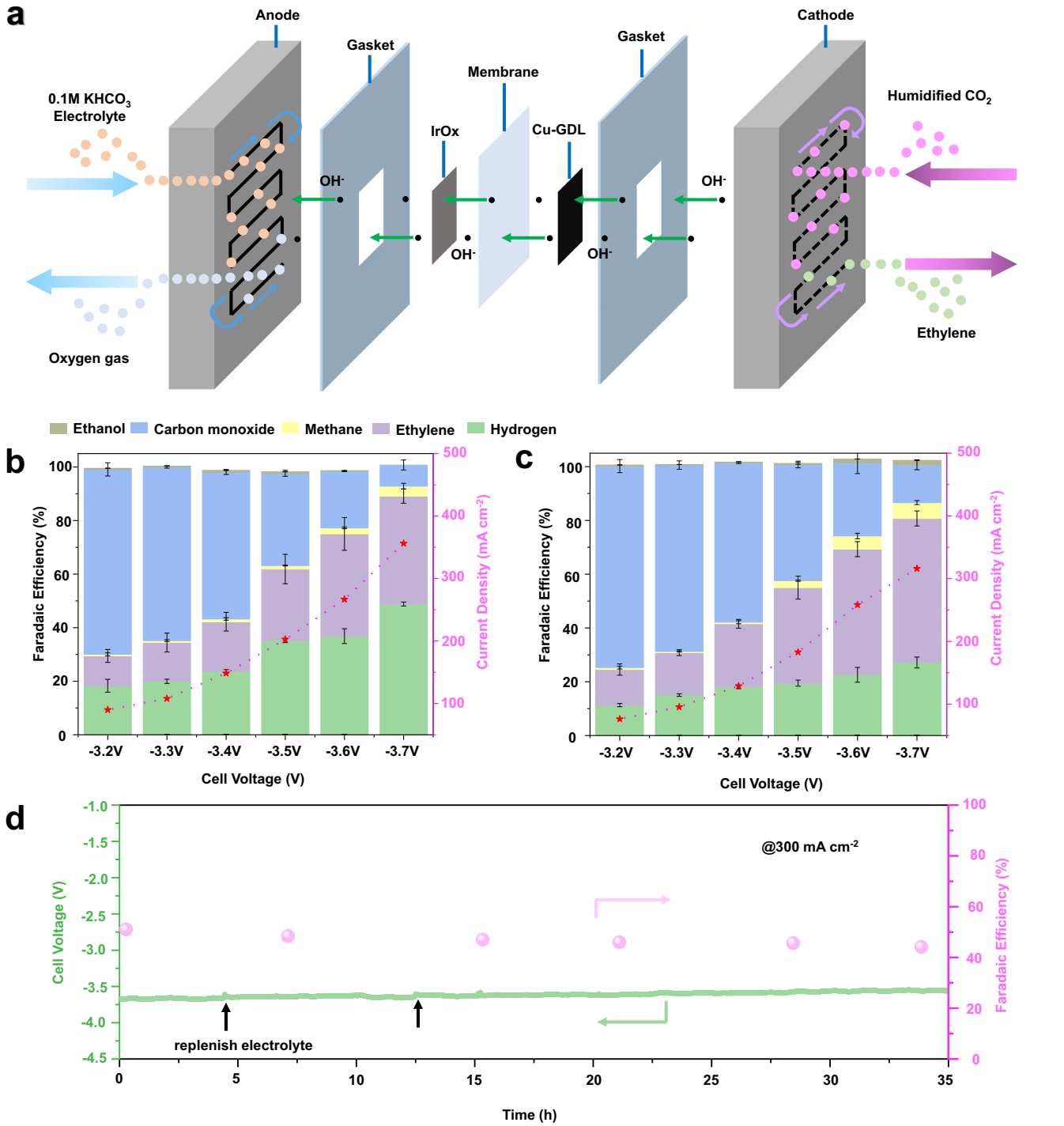

Fig. 1 | eCO_2RR performance of as-prepared catalysts. a Schematic of the MEA reactor. **b**, **c** eCO_2RR performance of **b** OH–Cu and **c** F–Cu catalysts in the 5 cm^2 MEA reactor. **d** The long-term stability test for F–Cu at a current density of 300 mA cm^{-2} (1.5 A). All applied potentials were not iR corrected ($R = 0.25 \pm 0.01\ \Omega$). Error bars represent the standard deviations calculated from three independent measurements.

Ex situ characterization of electrocatalysts

Ex situ scanning electron microscopy (SEM) images were taken to investigate the dynamic morphological and structural evolution of the catalysts. Cu NPs were sprayed onto GDEs, and their original morphology remained unchanged before the reaction (Fig. 2a and Supplementary Fig. 5a). After the MEA test, some nanowhiskers grew in situ on the GDEs, forming bundles and stacking on each other (Supplementary Fig. 5b, c). They had lengths of tens of micrometers and consisted of Cu, C, and O elements (Supplementary Fig. 5d–f). Similar morphological evolution and elemental distribution were observed in OH–Cu on GDEs (Supplementary Fig. 6). This indicates that carbon is involved in the structural evolution of the nanowhiskers, possibly originating from the GDEs, ACB, or CO_3^{2-} from $KHCO_3$ electrolyte. Compared to Cu NPs, the coverage of nanowhsikers on the GDEs in the OH–Cu sample was significantly higher, and their growth was more uniform without stacking (Supplementary Fig. 5b, c vs Supplementary

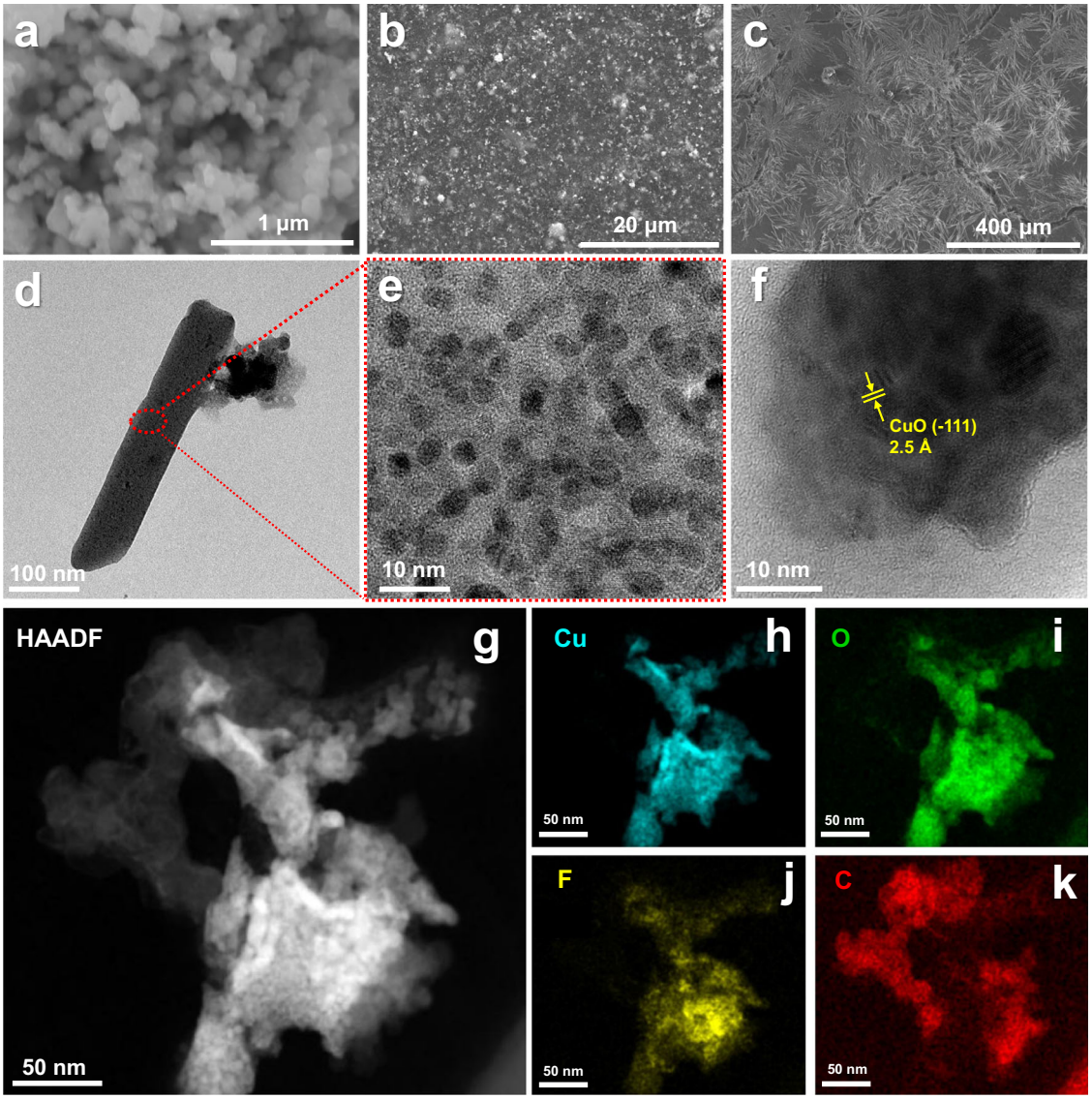

Fig. 2 | Characterizations of fresh and used electrocatalysts. a–c SEM images of **a** fresh Cu NPs, **b** fresh F–Cu on GDEs, and **c** used F–Cu on GDEs. **d** TEM images and **e** corresponding high-resolution TEM images of used F–Cu catalysts; **f**, **g** HAADF-STEM images and **h–k** corresponding EDS elemental mapping images of used F–Cu catalyst.

Fig. 6b, c). Both samples were tested under identical experimental conditions. This suggests that the carbon originates from the ACB, triggering structural evolution. This assumption is further confirmed by the F–Cu sample (Supplementary Fig. 7). Compared to OH–Cu (Supplementary Fig. 6a–c), the longer lengths (>50= μm) of nanowhiskers on the F–Cu sample indicate that the fluorination significantly enhances structural transformation (Fig. 2b, c and Supplementary Fig. 7), highlighting the major impact of functional groups on the surface of ACB on the structural evolution of nanowhiskers.

High-resolution transmission electron microscopy (HRTEM) and high-angle annular dark-field scanning TEM (HAADF-STEM) images provided deeper insights into the in situ reconstruction of Cu NPs at the nanometer scale. For example, in used F–Cu, 60–80 nm Cu NPs underwent potential-induced fragmentation, forming Cu nanoclusters with diameters of 3–6 nm after the eCO_2RR test in the MEA (Fig. 2d, e and Supplementary Fig. 8a–d). Subsequently, these nanoclusters oxidized upon exposure to air during ex situ characterization, resulting in the formation of CuO NPs (Fig. 2f and Supplementary Fig. 8c, d). Energy-dispersive X-ray spectroscopy (EDS) elemental mapping revealed a homogeneous distribution of Cu, O, F, and C atoms on the used F–Cu (Fig. 2g–k and Supplementary Fig. 9a–e). F–CB served as the substrate for the deposition of CuO NPs. Moreover, the morphological evolution of F–Cu was captured by ex situ SEM images under various cathodic potentials in the MEA. The 60–80 nm Cu NPs were held at −3.4 V and then underwent significant particle migration at −3.5 V (Fig. 3a). At this stage, the presence of nanowhiskers ~2.5 μm long indicated that the Cu NPs experienced initial particle reconstruction on the catalyst layer and subsequently grew into nanowhiskers with high length-to-diameter ratios (with 10 μm in length). Finally, raising the potentials promoted the growth of nanowhiskers (up to 50 μm), resulting in a uniform distribution of nanowhiskers on the surface of GDEs (Fig. 3a). Based on ex situ characterization analyses, we conclude that during eCO_2RR in the MEA reactor, the fragmented nanoparticles detach from the Cu matrix and rapidly evolve into well-defined nanoclusters attached to the carbon support. Subsequently, the potential-induced migration of nanoclusters leads to their structural transformation into nanowhiskers[23] (Fig. 3a, b).

Grazing incidence X-ray diffraction (GIXRD) was performed to investigate the changes in composition and structural features of samples before and after the reaction. The characteristic peaks at

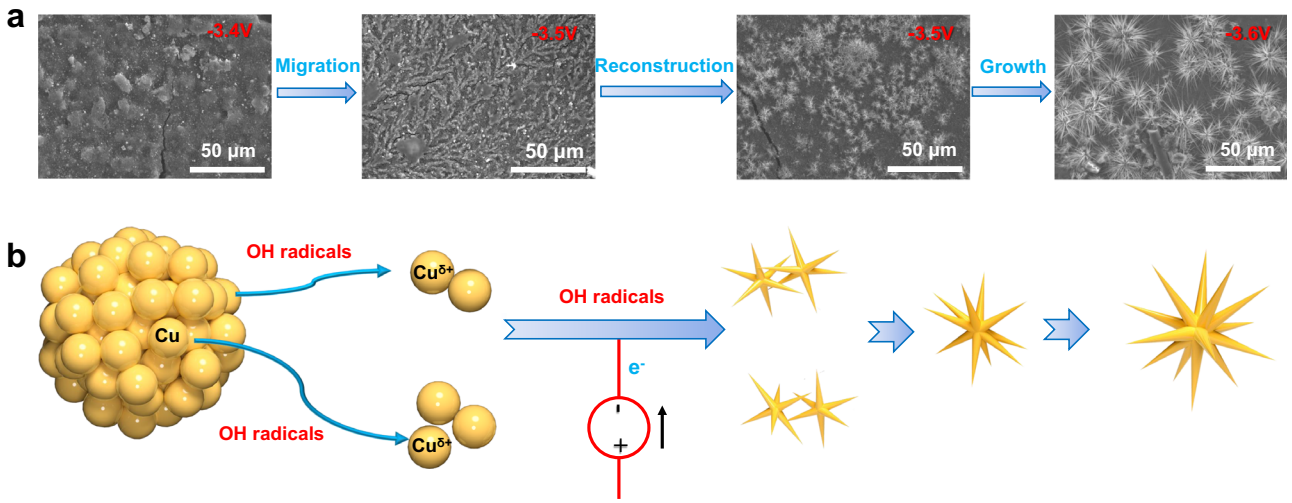

Fig. 3 | The structural evolution process of the catalyst during eCO$_2$RR in the MEA reactor. a Ex situ SEM images of structural evolution of F–Cu catalysts at negative potentials of −3.4 V, −3.5 V, and −3.6 V in the MEA reactor. **b** A schematic structural evolution mechanism for Cu NPs during eCO$_2$RR in the MEA reactor. All applied potentials were not iR corrected ($R = 0.25 \pm 0.01\ \Omega$).

43.2°, 50.4°, and 74.1° correspond to the (111), (200), and (220) reflections of Cu, respectively (Supplementary Fig. 10a)[24]. The Cu_2O peaks at (111) and (220) in all fresh samples indicated the oxidation of Cu[25]. GIXRD analysis revealed that before the reaction, the sample consisted of a mixture of Cu and Cu_2O (Supplementary Fig. 10a). However, after the eCO$_2$RR, when the sample was removed from the MEA and exposed to air for ex situ characterization, the unstable and active $Cu^{\delta+}$ species generated during eCO$_2$RR further oxidized to CuO. Due to the in situ growth of nanowhiskers on the GDEs, which underwent hydrophobic treatment with PTFE, and the CuO was encapsulated by the graphene-like ACB carrier formed during morphology reconstruction, it became challenging to obtain accurate phase information of the post-reaction sample (Supplementary Fig. 10b). However, conclusions drawn from STEM and TEM images in Fig. 2f, g and Supplementary Fig. 8c, d indicated that the intrinsic composition of the post-reaction sample was CuO loaded onto the ACB support.

X-ray photoelectron spectroscopy (XPS) was employed to investigate the surface compositions and chemical states of both fresh and used catalysts. The Cu $2p_{3/2}$ spectra of all fresh samples exhibited peaks at 933.4 and 935.2 eV, corresponding to Cu^+ or Cu^0 and Cu^{2+}, respectively (Supplementary Fig. 11a)[26]. The presence of Cu^{2+} species in all fresh samples was attributed to surface oxidation in air. The ACB significantly enhanced the intensity of the C = O bond at 532.4 eV, making it the dominant species in the O 1*s* spectra of F–Cu and OH–Cu, contrasting with the predominant lattice oxygen at 530.0 eV and the adsorbed O_2 in η_1(O) configuration (O_2^*) at 531.4 eV observed in Cu NPs (Supplementary Fig. 11b, c)[27]. After eCO$_2$RR, the Cu^+ or Cu^0 species were absent, and the Cu 2*p* peaks shifted to higher binding energy at ~935.3–936.1 eV (Fig. 4a). Theoretically, Cu species follow the binding energy trend: Cu^+ ions < Cu^{2+} ions < Cu(II) bound to extra-framework oxygen[28]. Since no Cu–F bond was observed at 684.4 eV in the F 1*s* spectra[29] (Supplementary Fig. 12a, b), the high binding energy in the Cu 2*p* spectra indicated that Cu species were bound to extra-framework oxygen atoms (Cu–OH). In contrast, both OH–Cu and F–Cu exhibited depletion of O_2^* species (531.4 eV) and lattice oxygen (530 eV) after the MEA test (Fig. 4b vs Supplementary Fig. 11b). This revealed that lattice oxygen did not convert into O_2 during structural transformation, as evidenced by the decrease in the O_2^* peak of used Cu NPs (Fig. 4b). Therefore, lattice oxygen converted to OH radicals after accepting electrons from Cu atoms, leading to a shift in the Cu 2*p* binding energy to higher values (Fig. 4a vs Supplementary Fig. 11a). Unlike used OH–Cu, the shift of the C=O bond peak to higher energy in used F–Cu highlighted the influence of fluorination (Fig. 4b). Additionally, owing to the numerous surface vacancies and hydrogen bonds, the water adsorbed at surface oxygen vacancy sites ($H_2O^*@O_{vac}$ at 533.2 eV) induced lattice rearrangement[27], resulting in structural transformation (Fig. 4b).

Cu K-edge X-ray absorption Near-Edge Structure (XANES) spectra and extended X-ray absorption fine structure (EXAFS) were collected to enhance understanding of the electronic structure and coordination environment of copper species in fresh and used samples (Fig. 4c, d). Compared to Cu foil, XANES spectra in Fig. 4c indicated that the Cu sites in all fresh samples were in an oxidized state ($Cu^{\delta+}$ species, $0 < \delta < 1$). For Cu NPs, copper oxidation may be attributed to exposure to air during ex situ characterization. With OH–CB and F–CB, the absorption edge of copper shifted to higher energy, indicating an interaction between the functional groups (OH and F) of ACB and the active copper sites. However, the oxidation state of copper in all used samples transitioned to a divalent state (Fig. 4c). This indicated that the eCO$_2$RR altered the overall structure and coordination environment of active copper sites in fresh samples, causing additional oxidation of unstable and active copper species during eCO$_2$RR to a divalent state upon exposed to air. Furthermore, regardless of whether samples are fresh or used, copper oxidation follows this sequence: fluorination effect > hydroxylation effect > no carbon black, highlighting the impact of functional groups on the copper structure. Notably, the valence state of Cu for Cu NPs shifted to divalent after MEA testing, even in the absence of ACB. This indicated that the change in the valence state was influenced by the eCO$_2$RR itself, rather than by the functional groups. The functional groups (F and OH) served solely as catalysts in promoting the valence evolution. Additionally, the EXAFS fitting data of fresh Cu NPs, OH–Cu, and F–Cu NPs revealed a Cu-Cu scattering path at ~2.52 Å (Fig. 4d, Supplementary Fig. 13a–c and Supplementary Table 2), and characteristic of metallic Cu. However, in fresh F–Cu, the Cu–Cu bonds transformed into Cu–O bonds after eCO$_2$RR testing in the MEA, reducing the coordination number from 10.3 (0.6) (Cu-Cu) before the eCO$_2$RR to 5.8 (0.5) (Cu–O) after eCO$_2$RR in the MEA (Fig. 4d, Supplementary Fig. 13d–f and Supplementary Table 2). Similar changes were observed in OH–Cu and Cu NPs, suggesting a uniform coordination environment among all tested samples. The oxidative species produced during eCO$_2$RR in the MEA destabilized active Cu sites, leading to changes in the valence state and coordination environment of Cu NPs. The functional groups from ACB

https://doi.org/10.1038/s41467-024-52004-2

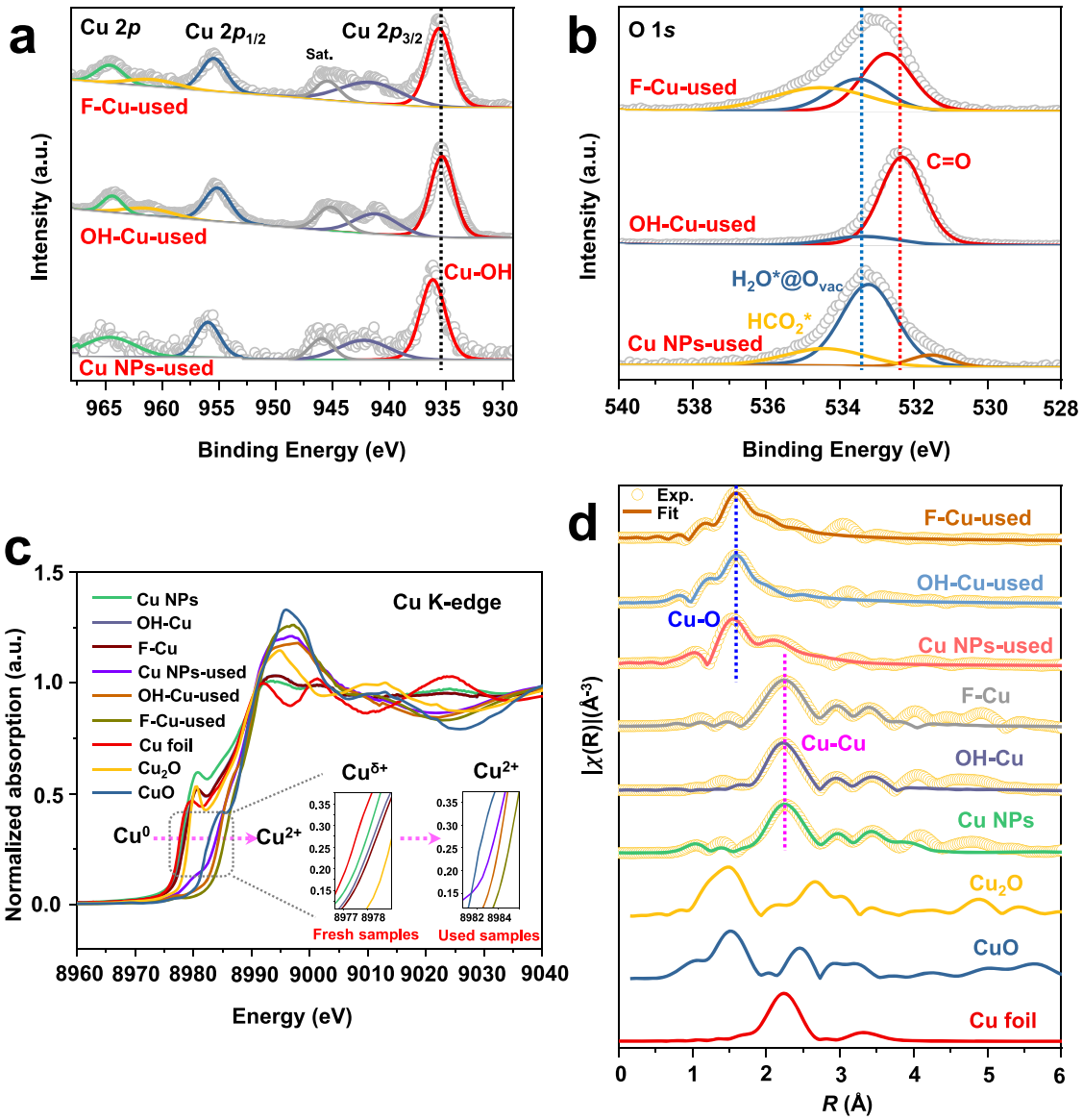

Fig. 4 | Ex situ X-ray spectroscopic analysis of electrocatalysts. a Cu 2*p* XPS spectra and **b** O 1*s* XPS spectra of used Cu NPs, OH–Cu, and F–Cu catalysts; **c** Cu K-edge XANES spectra and **d** Cu K-edge EXAFS experimental and fitting spectra of fresh and used Cu NPs, OH–Cu, and F–Cu samples and corresponding references (Cu foil, Cu_2O, and CuO).

(F and OH) exclusively facilitated the structural transformation of nanowhiskers.

In situ multimodal characterizations of electrocatalysts for eCO_2RR in neutral media

To enhance our understanding of eCO_2RR in an MEA reactor, in situ characterization techniques were crucial for monitoring the structural evolution of Cu species and investigating the formation of nanowhiskers. In situ Cu K-edge XANES spectra were recorded in CO_2-saturated 0.1 M $KHCO_3$ electrolyte while varying the cathodic potentials from −1 V to −3.5 V (Fig. 5a, b and Supplementary Figs. 14–17). Switching from cyclic voltammetry (CV) to open circuit potential (OCP) caused the oxidation state of Cu sites in Cu NPs to approach the Cu(I) state ($Cu^{\delta+}$, $0 < \delta < 1$) (Supplementary Fig. 16a). This indicated that highly oxidative radicals generated in situ in the pH-neutral electrolyte facilitated the rapid reoxidation of active Cu sites. A similar phenomenon was observed in OH–Cu (Supplementary Fig. 17a) and F–Cu (Fig. 5a). In situ potential-dependent XANES spectra were conducted to examine the stability of $Cu^{\delta+}$ species during eCO_2RR. Despite the reduction of $Cu^{\delta+}$ species in all samples with increasing negative potentials, dynamically generated $Cu^{\delta+}$ ($0 < \delta < 1$) species persisted as non-oxide-derived Cu sites during eCO_2RR (Fig. 5a, Supplementary Figs. 16a and 17a). Specifically, the $Cu^{\delta+}$ species in OH–Cu after eCO_2RR underwent a reduction and re-oxidation process in the neutral electrolyte over time (Supplementary Fig. 17a), indicating the persistence of strongly oxidative radicals in the pH-neutral electrolyte, which induced the spontaneous oxidation of Cu sites. Although Cu NPs were predominantly in their metallic state, the Cu nanoclusters formed during structural transformation were highly unstable. When exposed to air, H_2O adsorbed on surface defect sites and atmospheric oxygen can penetrate the structural network of nanowhiskers, accelerating the oxidation of $Cu^{\delta+}$ species to Cu(II) state. These findings are consistent with the observations from ex situ XANES spectra (Fig. 4c). Additionally, in situ Cu K-edge EXAFS spectra of Cu NPs showed mixed metallic Cu and oxidized $Cu^{\delta+}$ species at low cathodic potentials during eCO_2RR (Supplementary Fig. 16c). The strong reducing effect led to the reduction of $Cu^{\delta+}$ species, with only metallic Cu observed at high negative potentials (Supplementary Fig. 16c). As the negative

https://doi.org/10.1038/s41467-024-52004-2

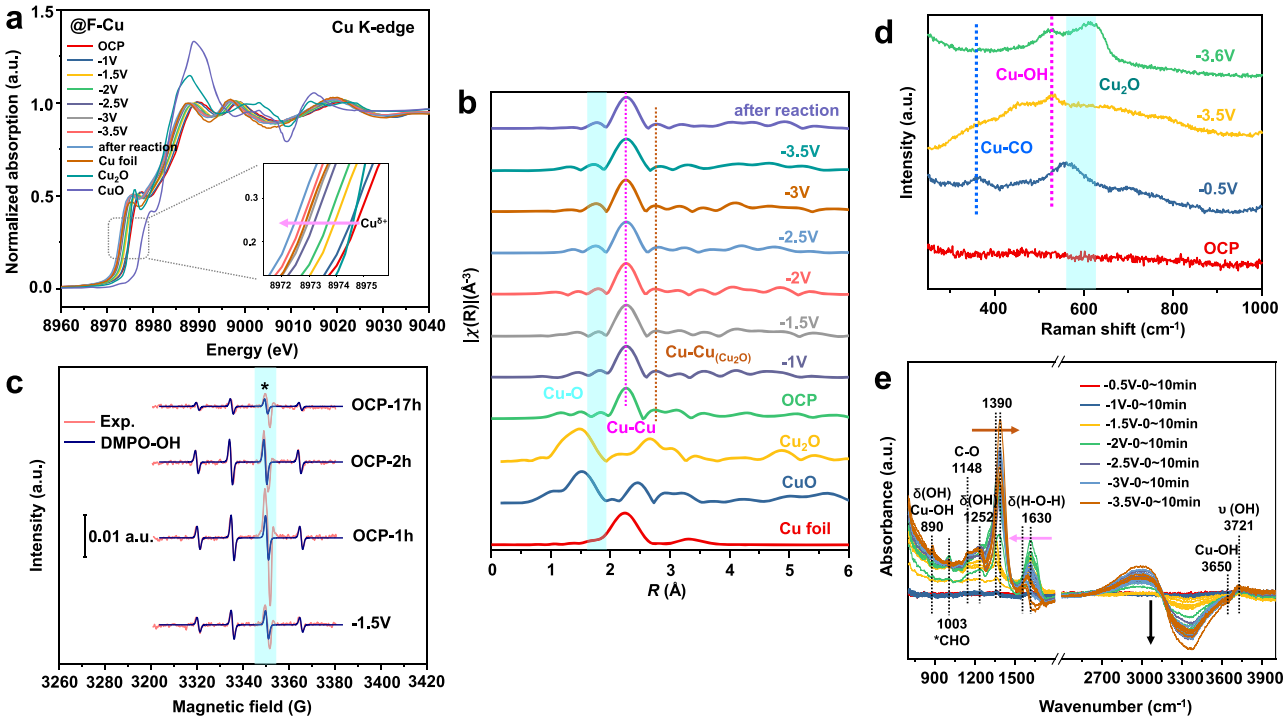

Fig. 5 | In situ multimodal characterizations of electrocatalysts during eCO_2RR in neutral media. a In situ Cu K-edge XANES spectra and **b** in situ Cu K-edge EXAFS spectra of F–Cu at different cathodic potentials (OCP, −1 V, −1.5 V, −2 V, −2.5 V, −3 V, −3.5 V, and after reaction). ($R = 212 \pm 5\ \Omega$). **c** In situ time-dependent normalized EPR spectra of F–Cu in CO_2-saturated 0.1 M $KHCO_3$ electrolyte at −1.5 V, followed by switching to OCP for different periods ($R = 212 \pm 5\ \Omega$). EPR signals marked by asterisk is from the sample tube. **d** In situ Raman spectra of F–Cu in CO_2-saturated 0.1 M $KHCO_3$ electrolyte at different potentials ($R = 181 \pm 3\ \Omega$). **e** In situ real-time ATR FT-IR spectra of F–Cu sample under different applied potentials ($R = 156 \pm 2\ \Omega$). All applied potentials were not iR corrected.

potentials increased, the Cu–Cu bond length in Cu NPs gradually increased, indicating fragmentation and migration of some Cu atoms from the Cu matrix under negative bias, contributing to structural reconstruction from nanoparticles to nanowhiskers. In contrast, OH–Cu (Supplementary Fig. 17c) and F–Cu (Fig. 5b) exhibited stabilized $Cu^{\delta+}$ species and metallic Cu after switching to OCP. Comparing the SEM images of the structural reconstruction of Cu NPs, OH–Cu, and F–Cu (Supplementary Figs. 5–7) revealed that the structural reconstruction of Cu NPs was primarily driven by the tensile strain effect on some metallic Cu sites resulting from the electric field and OH radicals. Hydroxylated $Cu^{\delta+}$ species play a crucial role in the large-scale and regular structural evolution of nanowhiskers in OH–Cu and F–Cu. The Cu–Cu bond length for Cu NPs was close to the initial value after eCO_2RR (Supplementary Fig. 16c), suggesting non-continuous evolution in Cu NPs. F–Cu (Fig. 5b) and OH–Cu (Supplementary Fig. 17c) still maintained oxidized $Cu^{\delta+}$ species after eCO_2RR, indicating continuous structural evolution in both samples, even without an electric field. Therefore, the mechanisms behind the structural evolution of Cu NPs differ from those of OH–Cu and F–Cu. For Cu NPs, the tensile strain effect induced by hydroxyl radicals detaches Cu atoms from the surface, contributing to structural transformation under negative bias. The involvement of functional groups in OH–Cu and F–Cu enhances the surface oxidative microenvironment of active Cu sites, increasing the production of oxidative radicals and stabilizing $Cu^{\delta+}$ species, thus inducing the uniform structural evolution of nanowhiskers under electric potentials.

In situ time-dependent electron paramagnetic resonance (EPR) spectra were conducted to confirm the presence of strongly oxidative radicals during eCO_2RR (Fig. 5c and Supplementary Fig. 18). The F–Cu catalyst underwent a 20-min eCO_2RR at −1.5 V before electrolyte collection to mitigate the impact of residual oxidative species in the CO_2-saturated 0.1 M $KHCO_3$ electrolyte containing 10 mM 5,5-dimethyl-1-pyrroline N-oxide (DMPO). OH radicals ($A_N = 1.50$ mT, $A_H = 1.48$ mT) rather than hydrogen radicals, were produced during eCO_2RR, differing from previous studies[30]. The in situ-generated strongly oxidative OH radicals can induce the oxidation of active Cu species during eCO_2RR. This indicated that a locally oxidative microenvironment on the catalyst surface facilitated the C–C coupling for C_2H_4 production, even in a neutral electrolyte. Upon switching to OCP, the OH radicals in the electrolyte did not diminish, and their persistent presence after the eCO_2RR reaction stabilized active $Cu^{\delta+}$ species, further inducing the structural evolution of catalysts. This finding agrees with in situ XAS spectra results (Fig. 5a, b and Supplementary Fig. 17).

The presence of an oxygenated Cu surface during eCO_2RR was further confirmed by the in situ Raman spectra (Supplementary Fig. 19). Ex situ SEM images tracked the morphological changes during eCO_2RR in the Raman cell, correlating with MEA reactor conditions. Similar structural evolution was confirmed (Supplementary Fig. 20). Initially, $Cu^{\delta+}$ species clustered in islands near GDEs cracks. Subsequently, structural evolution began at the center and edges of the island. Accumulated $Cu^{\delta+}$ species from the bulk phase promoted rapid nanowhisker growth, covering the entire area. This morphological transformation highlights the relevance of our in situ Raman characterization to actual eCO_2RR in the MEA reactor. In the Raman spectra of F–Cu (Fig. 5d and Supplementary Fig. 21a), peaks at 565.2 cm^{-1} (Cu_2O)[30], 364 cm^{-1} (Cu–CO)[10], 1073.5 cm^{-1} (CO_3^{2-})[30], and 1522 cm^{-1} (C=C stretching from CO_2)[31] emerged at −0.5 V. The absence of $Cu^{\delta+}$–OH species indicated no morphology reconstruction at low potentials. However, surface $Cu^{\delta+}$–OH species at 532 cm^{-1}[10] became predominant at −3.5 V (Fig. 5d), suggesting the onset of structural evolution. At −3.6 V, a Cu_2O peak reappeared (Fig. 5d), further driving the structural transformation of nanowhiskers. After eCO_2RR, these oxidized $Cu^{\delta+}$ species (Cu–OH, Cu_2O) underwent additional oxidation to form CuO (Supplementary Fig. 21b), consistent with observations from HRTEM,

HADDF-STEM, and ex situ XAS spectra (Fig. 2f, Fig. 4c, d and Supplementary Fig. 8c, d). Furthermore, the resistance of $Cu^{\delta+}$ (Cu–OH, Cu_2O) species to reduction under high cathodic potentials indicates that the stabilized $Cu^{\delta+}$ species are the actual active sites during eCO_2RR, while changes in morphology enhance eCO_2RR-to-C_2H_4 conversion. Additionally, prior studies have shown that F doping can regulate the electronic structure of the active site to optimize the eCO_2RR performance[32,33]. Therefore, we investigated the impact of F-CB by analyzing the in situ Raman spectra of Cu NPs (Supplementary Fig. 21c). We found that while Cu NPs showed Raman peaks similar to F–Cu (Cu–CO and Cu_2O) at low potentials, Cu–OH species were absent at high potentials. Comparison of the structural evolution of Cu NPs and F–Cu (Supplementary Fig. 5 vs Supplementary Fig. 7) indicated that F–CB altered the interfacial microenvironment of Cu NPs, enhancing the structural transformation with $Cu^{\delta+}$–OH species playing a critical role. F-functional groups can activate water, enriching strongly oxidative OH radicals on the Cu surface, thereby stabilizing $Cu^{\delta+}$ species. We conclude that $Cu^{\delta+}$–OH species are not involved in reconstruction under low electric fields, resulting in a reversible process, despite the detection of $Cu^{\delta+}$ (Cu_2O and Cu-CO) species during eCO_2RR. Conversely, under high electric fields, $Cu^{\delta+}$ ($Cu^{\delta+}$–OH) species are generated; surface defects and functional groups from ACB act as kinetically trapped sites, facilitating the migration of $Cu^{\delta+}$ species from bulk to the support surface. In situ-generated, strongly oxidative OH radicals stabilize oxidized $Cu^{\delta+}$ species in nanowhiskers, ultimately leading to irreversible structural reconstruction under high bias.

Real-time ATR FT-IR spectra were employed to monitor intermediate adsorption processes at the electrode-electrolyte interface. Spectra were collected every two minutes during potential application and after potential cessation in a CO_2-staturated 0.1 M $KHCO_3$ solution (Fig. 5e and Supplementary Figs. 22 and 23). Referring to in situ ATR FT-IR spectra of Cu NPs (Supplementary Fig. 23a), only a few intermediate peaks related to eCO_2RR were detected, likely due to multiple reaction pathways and low intermediate concentrations. In contrast, the F–Cu sample showed more prominent adsorption bands at 1003 cm^{-1} and 1148 cm^{-1}, attributed to the $^*CHO$ and the C–O bond vibration mode[34,35], respectively. These are recognized as key intermediates in the C–C coupling during eCO_2RR to C_2H_4 (Fig. 5e). Furthermore, increasing cathodic potentials resulted in higher intensity of intermediate adsorption on the F–Cu surface, indicating the potential-dependent nature of eCO_2RR reaction rates. Additionally, a broad adsorption band related to H-bonded hydroxyl groups appeared in the 2500–3600 cm^{-1} range, accompanied by adsorbed water (δ(H–O–H)) at 1630 cm^{-1} (Fig. 5e)[36]. These bands are indicative of perturbed water molecules under negative potentials. However, extra-ligand OH exhibited stretching vibration modes of ν(OH) at 3721 cm^{-1} and δ(OH) at 1252 cm^{-1}[36,37], on the external surfaces of F–Cu (Fig. 5e), primarily due to the contribution of framework modes. This indicated the presence of a metal ionic site (e.g., $Cu^{\delta+}$ species). Thus, the bands at 890 cm^{-1} and 3650 cm^{-1} were considered characteristic features of $Cu^{\delta+}$–OH species stabilized in the ν(OH) and δ(OH) modes[38,39], respectively. Again, this underscored the crucial role of hydroxyl species as oxidants for $Cu^{\delta+}$ species (Fig. 5e). Although Cu NPs also exhibited infrared peaks corresponding to $Cu^{\delta+}$–OH species, there was no disturbance observed in the vibrations of water molecules at 1620 cm^{-1} (Supplementary Fig. 23a). This further indicated that the introduction of F-functional groups enhanced the activation and splitting of water molecules, facilitating Cu binding with OH species.

Intermediate adsorption processes were recorded to elucidate the origin of hydroxyl species (Fig. 5e and Supplementary Fig. 23b–f). Bands showing significant changes were marked with dotted lines and arrows. With increasing applied potentials, the vibrational modes of bicarbonate at 1360 cm^{-1} gradually shifted toward a broader band centered on the asymmetric C–O stretch of carbonate at 1390 cm^{-1}[40]. This was explained by the increase in OH radicals at the cathodic electrode interface during water reduction, which reduced adsorbed bicarbonate and increased carbonate under more negative potentials. This hypothesis was further confirmed by water molecule perturbations. Increasing cathodic potentials shifted δ(H–O–H) from 1630 cm^{-1} to 1575 cm^{-1} with decreased intensity, indicating that water dissociation produced more OH radicals to stabilize $Cu^{\delta+}$ species, particularly under high negative potentials. Moreover, the higher intensity of $Cu^{\delta+}$–OH and extra-ligand OH species with increasing potentials revealed changes in the surface structure. Additionally, the mechanism of depopulation of intermediates was investigated (Supplementary Fig. 23b–f). At a low cathodic potential of −1.5 V, the bicarbonate band at 1359 cm^{-1} remained unchanged, while the δ(H–O–H) band slightly shifted. These peaks gradually disappeared after the potentials were turned off, but the in situ-generated eCO_2RR intermediates disappeared immediately. Further increasing the potential resulted in a greater shift for bicarbonate and stronger perturbations of water molecules, but they gradually returned to the initial stage when the potentials were removed. Furthermore, extra-ligand OH species were unlikely to stabilize on active $Cu^{\delta+}$ sites after eCO_2RR under high negative potentials. Instead, water molecules coordinated with $Cu^{\delta+}$ species to form aqua complexes and maintained a specific configuration. When exposed to air, it gradually oxidized to CuO.

Based on the above analysis, OH radicals can create a locally oxidative microenvironment on the Cu surface during eCO_2RR, stabilizing $Cu^{\delta+}$ species and enhancing C_2H_4 selectivity. Although in situ Raman spectroscopy, EPR spectra, ATR FT-IR spectroscopy, and XAS spectra can directly detect $Cu^{\delta+}$-OH species, the significant difference in current densities between in situ electrochemical cell and MEA reactor precludes accurate simulation of catalyst evolution in an MEA. This is because the rapid kinetics of the eCO_2RR at high current densities introduce gas bubbles that critically affect data acquisition. Furthermore, in the MEA reactor, the catalyst layer on the GDEs is closely attached to the AEM, preventing direct monitoring of surface structural changes of the catalyst using Raman, infrared, and EPR spectroscopy. XAS spectroscopy could be a feasible method for monitoring changes in the oxidation state and coordination environment of copper during the MEA testing. However, to gain more structural insights, future endeavors should focus on rationally designing in situ MEA cells and conducting coordinated multimodal characterization studies to elucidate the evolution of active sites.

Discussion

In summary, functionalized ACB was introduced to modulate the interfacial microenvironment of Cu NPs in the pH-neutral electrolyte. The enhanced performance of eCO_2RR to C_2H_4 (55.6% ± 2.8 FE at 316 mA cm^{-2}) in an MEA reactor was attributed to the locally oxidative microenvironment on the catalyst surface, regulated by hydroxyl species generated in situ from water dissociation. The well-stabilized $Cu^{\delta+}$–OH species induced the fragmentation of Cu NPs from the Cu matrix and their migration on the carbon support under high negative bias, resulting in an irreversible and asynchronous change in morphology and valence, yielding high-curvature structure (nanowhiskers). Understanding the reaction mechanism in an MEA electrolyzer would better guide the redesign and assembly of catalysts on the GDEs within MEA, accelerating the commercialization of eCO_2RR.

Methods

Chemicals and materials

Cu NPs (60–80 nm in diameter, ≥99.5%), iridium (III) chloride hydrate ($IrCl_3•xH_2O$, 99.9%) and potassium bicarbonate ($KHCO_3$, 99.7%) were purchased from Sigma-Aldrich, Canada. Potassium hydroxide (KOH, ≥85%), Sodium hydroxide (NaOH, ≥97%), ammonium fluoride (NH_4F, ≥98%), oxalic acid (98%), hydrochloric acid (HCl, 37%), isopropanol (≥99%), and ultrapure water (18 MΩ cm) were obtained from the

University of Waterloo Chemical Store. Carbon black-Vulcan XC 72, titanium fiber felt, and Sigracet 39BB were purchased from fuel cell store, USA. Sustainion® anion exchange membrane (Sustainion® X37-50 Grade RT membrane) with 50 microns was sourced from Dioxide Materials, USA. All materials except Sustainion® X37-50 Grade RT Membrane, were used as received without further purification. Prior to use, the Sustainion® X37-50 Grade RT Membrane was cut into 4 × 4 cm pieces and activated in a 1 M KOH solution for 12 h.

Synthesis of cathodic OH−Cu electrocatalysts

For typical activation of carbon black[26], 0.2 g of carbon black was treated by 100 mL of 2 M NaOH solution with continuous stirring for 24 h at room temperature. The resulting suspension was centrifuged and washed three times with water until reaching constant pH. The synthesized sample was designated as OH−CB. The mixture of OH−CB and Cu NPs (mass ratio = 1:1) was named as OH−Cu.

Synthesis of cathodic F−Cu electrocatalysts

For the fluorination of carbon black, 0.1 g of the prepared OH−CB samples were dispersed in 70 mL isopropanol under ultrasonication, followed by addition of 0.5 g of NH_4F into the mixture. After continuous ultrasonication for 1 h, the solution was transferred into an autoclave and kept at 120 °C for 20 h. The precipitate was centrifuged, washed three times with water, and dried in a vacuum at 60 °C for 12 h. The sample was designated as F−CB. The mixture of F−CB and Cu NPs (mass ratio = 1:1) was named as F−Cu.

Synthesis of anode IrO_x/Ti electrocatalysts

IrO_x/Ti fiber felt was synthesized by a dip coating and thermal decomposition method[41]. Ti fiber felt was etched with boiling 0.5 M oxalic acid for 60 min, and 30 mg of $IrCl_3{\bullet}xH_2O$ was dissolved in a 10 mL of 10% volume concentrated HCl-isopropanol solution. The Ti fiber felt obtained was then dip-coated in the above solutions, dried at 100 °C for 10 min, and calcined at 500 °C for 10 min in air. This procedure was repeated multiple times to achieve a loading of 0.5 mg.

Ex situ material characterizations

Scanning electron microscopy (SEM, Hitachi S4800, Japan) images were collected at an accelerating voltage of 10 kV. Grazing-incidence X-ray diffraction (GIXRD) measurements were performed under an MRD diffractometer (PANalytical X'Pert Pro, Netherlands) with Cu Kα radiation (1.54 Å) at an incidence angle of 0.6°. X-ray photoelectron spectroscopy (XPS) (Thermo-VG Scientific ESCALab 250, USA) spectra were collected by microprobes with a monochromatic Al Kα X-ray source (1486.6 eV). High-angle annular dark-field scanning transmission electron microscopy (HAADF-STEM) and energy dispersive X-ray spectroscopy (EDS) images (FEI Titan 80–300 HB TEM/STEM, USA) were performed using an aberration corrector at an accelerating voltage of 60 kV. High-resolution TEM tests (Zeiss Libra 200MC, German) were conducted at an acceleration voltage of 200 kV. Proton nuclear magnetic resonance (H-NMR) (Bruker Avance III 500 MHz, USA) was employed to analyze liquid products.

Electrochemical measurements

All electrochemical measurements were connected to a potentiostat (Gamry Reference 3000 electrochemical workstation, USA) at room temperature without iR compensation. All electrochemical data were automatically saved and processed using Gamry analysis software. A homemade 5 cm^2 MEA functioned as a dual-electrode zero-gap cell, with an anion exchange membrane (Sustainion® X37-50 Grade RT membrane) sandwiched between the anode and cathode. The electrolyte circulated through the porous anode without the use of a reference electrode. All applied potentials were not iR corrected. Prior to conducting the MEA test, 500 mL of 0.1 M $KHCO_3$ electrolyte (pH = 8.3 ± 0.2) was prepared and stored at room temperature. For electrode fabrication, 5 mg of catalyst was mixed with 1 mL isopropanol and 20 µl Nafion solution (5 wt%, Sigma-Aldrich), followed by sonication of 99 min to form a homogenous solution. The obtained catalyst ink was air-brushed onto gas diffusion electrodes (GDEs, Sigracet 39BB) (5 cm^2) and dried in the air. The loading of the catalyst was 1 mg/cm^2, and the area in contact with the membrane was 5 cm^2. IrOx/Ti fiber belt was used as the anode. The flow rate of CO_2 was controlled using a mass flow controller (0–100 sccm, Alicat Scientific, USA). The cathode side was supplied with a humidified CO_2 stream at a flow rate of 30 sccm, while the anode was circulated with 50 mL of 0.1 M $KHCO_3$ electrolyte at a flow rate of 18 mL min^{-1}. Gas products were quantified using an Agilent 6890 gas chromatograph (GC) equipped with a Carbonxen® 1000 column and a CarbonPLOT column for the flame ionization detector and thermal conductivity detector, respectively. The liquid products were analyzed using a Bruker 500 MHz Nuclear Magnetic Resonance (NMR) with an internal reference of D_2O and DMSO. The FEs for gas and liquid products were calculated as follows: $FE = eF \times n/Q = eF \times n/(I \times t)$, where e is number of transferred electrons, F is the Faraday constant, Q is the charge, I is the current, t is the testing time, and n is the total amount of product (in moles).

In situ XAS measurements

The measurements were conducted at 06ID-1 Hard X-ray Micro-Analysis (HXMA) beamline of the Canadian Light Source (CLS), operated at 2.9 GeV with a constant current of 250 mA. Measurements at the copper K-edge were performed in fluorescence mode using a Lytle detector. The customized in situ electrochemical cell consists of two chambers separated by an anion exchange membrane (Sustainion® X37-50 Grade RT membrane). The cathode chamber is equipped with a thin-layer, adjustable electrolyte structure. F−Cu GDEs with a loading of 1 mg/cm^2, a platinum foil, and an Ag/AgCl electrode were used as the working electrode, counter electrode, and reference electrode, respectively. Both the cathode and anode chambers were supplied with 50 mL of CO_2-saturated 0.1 M $KHCO_3$ electrolyte (pH = 6.8 ± 0.3) at a flow rate of 18 mL/min. In situ XAS measurements were recorded at applied cathodic potential ranging from −1 V to −3.5 V. All applied potentials were not iR corrected. The XAS data were fitted using the software package Athena.

In situ time-dependent EPR measurements

Time-dependent continuous-wave (CW) EPR measurements at X-band frequencies (9.4 GHz) were performed using a Bruker EMX Micro EPR spectrometer. DMPO was used as a spin trap. The electrochemical cell used for in situ EPR testing is the same as that used for the in situ XAS setup. All electrochemistry procedures are identical, except that the electrochemical test was performed in a CO_2-saturated 0.1 M $KHCO_3$ electrolyte (pH = 6.8 ± 0.3) containing 10 mM of DMPO. During eCO_2RR, 10 µL of samples were taken from the electrochemical cell and transferred into 1 mm ID, 2 mm OD EPR tube (712-SQ-100M Wilmad LabGlass). For EPR measurements, these tubes were placed into 3 mm ID 4 mm OD EPR tubes (707-SQ-250M Wilmad LabGlass). For all the measurements, the microwave power was set to 1.262 mW (22 dB microwave power attenuation) and modulation amplitude was 2 G at a modulation frequency of 100 kHz. EPR spectra were simulated using EasySpin software[42].

In situ ATR FT-IR measurements

Measurements were conducted at 02B1-1 Far-IR beamline of the Canadian Light Source (CLS). In situ ATR FT-IR spectroscopy was performed using a Bruker IFS 125 HR spectrometer with a custom-built Veemax III variable angle reflectance system (Pike Technologies, USA), and all spectra were presented as the absorbance [$-\log(R/R_0)$]. The catalyst ink was pipetted onto an ITO-coated SI Microgrooved Wafer Element with a 55° Face angle and dried in air before testing. A

platinum wire and an Ag/AgCl electrode were used as counter and reference electrodes, respectively, in a customized single-chamber electrochemical cell. The 10 mL of 0.1 M $KHCO_3$ electrolyte (pH = 6.8 ± 0.3) was continuously purged with CO_2 during the measurement. The applied cathodic potentials ranged from −0.5 V to −3.5 V, and infrared spectra were collected during eCO_2RR. All applied potentials were not iR corrected.

In situ Raman spectroscopy

Raman spectra were recorded using a Renishaw inVia Reflex system equipped with a 100× objective and a 633 nm excitation (Renishaw HeNe laser, 17 mW). The filter was set at 5% of maximum intensity. Measurements were performed in a customized dual-chamber gas diffusion Raman electrochemical cell with a quartz window. The cathode and anode chambers were separated by an anion exchange membrane (Sustainion® X37-50 Grade RT membrane). The as-prepared catalysts on GDEs, Ag/AgCl, and platinum wire served as the working, reference, and counter electrodes, respectively. The 50 mL of 0.1 M $KHCO_3$ electrolyte (pH = 6.8 ± 0.3) was constantly purged with a CO_2 gas flow rate of 30 sccm. The raw data were processed using the Renishaw WiRE 5.3 software package, including baseline subtraction, normalization, and curve fitting. All applied potentials were not iR corrected.

The resistance measurements of electrochemical cell

Potentiostatic electrochemical impedance spectroscopy (EIS) was conducted using a potential range of −5 V to 5 V, 100 kHz frequency, and a sinus amplitude of 10 mV. The calculated cell resistances for different setups were as follows: 0.25 ± 0.01 Ω for the MEA reactor, 212 ± 5 Ω for the electrochemical cell used for in situ XAS and in situ EPR, 181 ± 3 Ω for the in situ Raman electrochemical cell, and 156 ± 2 Ω for in situ ATR FT-IR electrochemical cell. It should be noted that in this paper, all reported potentials were not iR corrected.

The reference electrode calibration

For the typical calibration of an Ag/AgCl reference electrode[43], a three-electrode system was employed, with a Pt foil serving as both the working and the counter electrode. The 0.1 M Na_2SO_4 electrolyte was saturated with high-purity H_2 for at least 30 min before electrode calibration. CV was performed at a scan rate of 1 mV/s, and the average of two interconversion point values was taken as the thermodynamic potential.

Data availability

The authors declare that all data supporting this study are available within the paper and Supplementary Information files. Source data are provided with this paper.

References

1. Bushuyev, O. S. et al. What should we make with CO2 and how can we make it? *Joule* **2**, 825–832 (2018).
2. Nitopi, S. et al. Progress and perspectives of electrochemical CO2 reduction on copper in aqueous electrolyte. *Chem. Rev.* **119**, 7610–7672 (2019).
3. Zheng, T. et al. Large-scale and highly selective CO2 electrocatalytic reduction on nickel single-atom catalyst. *Joule* **3**, 265–278 (2019).
4. Popović, S. et al. Stability and degradation mechanisms of copper-based catalysts for electrochemical CO2 reduction. *Angew. Chem.* **132**, 14844–14854 (2020).
5. Fan, L. et al. Strategies in catalysts and electrolyzer design for electrochemical CO2 reduction toward C2+ products. *Sci. Adv.* **6**, eaay3111 (2020).
6. Chen, C., Li, Y. & Yang, P. Address the "alkalinity problem" in CO2 electrolysis with catalyst design and translation. *Joule* **5**, 737–742 (2021).
7. Dinh, C.-T. et al. CO2 electroreduction to ethylene via hydroxide-mediated copper catalysis at an abrupt interface. *Science* **360**, 783–787 (2018).
8. Zhang, X. et al. Selective and high current CO2 electro-reduction to multicarbon products in near-neutral KCl electrolytes. *J. Am. Chem. Soc.* **143**, 3245–3255 (2021).
9. Cao, Y. et al. Surface hydroxide promotes CO2 electrolysis to ethylene in acidic conditions. *Nat. Commun.* **14**, 2387 (2023).
10. Wang, Z. et al. Localized alkaline environment via in situ electrostatic confinement for enhanced CO2-to-ethylene conversion in neutral medium. *J. Am. Chem. Soc.* **145**, 6339–6348 (2023).
11. Ma, W. et al. Electrocatalytic reduction of CO2 to ethylene and ethanol through hydrogen-assisted C–C coupling over fluorine-modified copper. *Nat. Catal.* **3**, 478–487 (2020).
12. Endrődi, B. et al. Continuous-flow electroreduction of carbon dioxide. *Prog. Energy Combust. Sci.* **62**, 133–154 (2017).
13. Zheng, T. et al. Copper-catalysed exclusive CO2 to pure formic acid conversion via single-atom alloying. *Nat. Nanotechnol.* **16**, 1386–1393 (2021).
14. Xie, M. S. et al. Amino acid modified copper electrodes for the enhanced selective electroreduction of carbon dioxide towards hydrocarbons. *Energy Environ. Sci.* **9**, 1687–1695 (2016).
15. Zhou, Y. et al. Dopant-induced electron localization drives CO2 reduction to C2 hydrocarbons. *Nat. Chem.* **10**, 974–980 (2018).
16. Ledezma-Yanez, I., Gallent, E. P., Koper, M. T. & Calle-Vallejo, F. Structure-sensitive electroreduction of acetaldehyde to ethanol on copper and its mechanistic implications for CO and CO2 reduction. *Catal. Today* **262**, 90–94 (2016).
17. Lei, Q. et al. Structural evolution and strain generation of derived-Cu catalysts during CO2 electroreduction. *Nat. Commun.* **13**, 4857 (2022).
18. Lv, X. et al. Electron-deficient Cu sites on Cu3Ag1 catalyst promoting CO2 electroreduction to alcohols. *Adv. Energy Mater.* **10**, 2001987 (2020).
19. Mistry, H. et al. Highly selective plasma-activated copper catalysts for carbon dioxide reduction to ethylene. *Nat. Commun.* **7**, 1–9 (2016).
20. Liang, Z.-Q. et al. Copper-on-nitride enhances the stable electrosynthesis of multi-carbon products from CO2. *Nat. Commun.* **9**, 1–8 (2018).
21. Lum, Y. & Ager, J. W. Stability of residual oxides in oxide-derived copper catalysts for electrochemical CO2 reduction investigated with 18O labeling. *Angew. Chem. Int. Ed.* **57**, 551–554 (2018).
22. Yang, Y. et al. Operando studies reveal active Cu nanograins for CO2 electroreduction. *Nature* **614**, 262–269 (2023).
23. Li, F. et al. Interplay of electrochemical and electrical effects induces structural transformations in electrocatalysts. *Nat. Catal.* **4**, 479–487 (2021).
24. Gu, Z. et al. Oxygen vacancy tuning toward efficient electrocatalytic CO2 reduction to C2H4. *Small Methods* **3**, 1800449 (2019).
25. Li, D. et al. MOF-derived Cu2O/Cu nanospheres anchored in nitrogen-doped hollow porous carbon framework for increasing the selectivity and activity of electrochemical CO2-to-formate conversion. *ACS Appl. Mater. Interfaces* **12**, 7030–7037 (2020).
26. Wang, M. et al. Electrochemical reduction of CO2 on copper-based electrocatalyst supported on MWCNTs with different functional groups. *Energy Fuels.* **36**, 5833–5842 (2022).
27. Trinh, Q. T., Bhola, K., Amaniampong, P. N., Jerome, F. & Mushrif, S. H. Synergistic application of XPS and DFT to investigate metal oxide surface catalysis. *J. Phys. Chem. C* **122**, 22397–22406 (2018).
28. Artiglia, L. et al. In Situ X-ray photoelectron spectroscopy detects multiple active sites involved in the selective anaerobic oxidation of methane in copper-exchanged zeolites. *ACS Catal.* **9**, 6728–6737 (2019).

29. Sun, L., Peng, C., Kong, L., Li, Y. & Feng, W. Interface-structure-modulated CuF2/CF x composites for high-performance lithium primary batteries. *Energy Environ. Mater.* **6**, e12323 (2023).
30. Mu, S. et al. Hydroxyl radicals dominate reoxidation of oxide-derived Cu in electrochemical CO2 reduction. *Nat. Commun.* **13**, 3694 (2022).
31. Zhao, Y. et al. Elucidating electrochemical CO 2 reduction reaction processes on Cu (hkl) single-crystal surfaces by in situ Raman spectroscopy. *Energy Environ. Sci.* **15**, 3968–3977 (2022).
32. Ko, Y.-J. et al. Exploring dopant effects in stannic oxide nanoparticles for CO2 electro-reduction to formate. *Nat. Commun.* **13**, 2205 (2022).
33. Xie, J. et al. Metal-free fluorine-doped carbon electrocatalyst for CO2 reduction outcompeting hydrogen evolution. *Angew. Chem. Int. Ed.* **57**, 9640–9644 (2018).
34. Yi, J. D. et al. Highly selective CO2 electroreduction to CH4 by in situ generated Cu2O single-type sites on a conductive MOF: stabilizing key intermediates with hydrogen bonding. *Angew. Chem. Int. Ed.* **59**, 23641–23648 (2020).
35. Xie, H. et al. Achieving highly selective electrochemical CO2 reduction to C2H4 on Cu nanosheets. *J. Energy Chem.* **79**, 312–320 (2023).
36. Borfecchia, E. et al. Revisiting the nature of Cu sites in the activated Cu-SSZ-13 catalyst for SCR reaction. *Chem. Sci.* **6**, 548–563 (2015).
37. Zhang, R. et al. Photocatalytic oxidative dehydrogenation of ethane using CO2 as a soft oxidant over Pd/TiO2 catalysts to C2H4 and syngas. *ACS Catal.* **8**, 9280–9286 (2018).
38. Iwasaki, M. & Shinjoh, H. NO evolution reaction with NO2 adsorption over Fe/ZSM-5: In situ FT-IR observation and relationships with Fe sites. *J. Catal.* **273**, 29–38 (2010).
39. Giordanino, F. et al. Characterization of Cu-exchanged SSZ-13: a comparative FTIR, UV-Vis, and EPR study with Cu-ZSM-5 and Cu-β with similar Si/Al and Cu/Al ratios. *Dalton Trans.* **42**, 12741–12761 (2013).
40. Wang, L., Gupta, K., Goodall, J. B., Darr, J. A. & Holt, K. B. In situ spectroscopic monitoring of CO 2 reduction at copper oxide electrode. *Faraday Discuss* **197**, 517–532 (2017).
41. Luc, W., Rosen, J. & Jiao, F. An Ir-based anode for a practical CO2 electrolyzer. *Catal. Today* **288**, 79–84 (2017).
42. Stoll, S. & Schweiger, A. EasySpin, a comprehensive software package for spectral simulation and analysis in EPR. *J. Magn. Reson.* **178**, 42–55 (2006).
43. Niu, S., Li, S., Du, Y., Han, X. & Xu, P. How to reliably report the overpotential of an electrocatalyst. *ACS Energy Lett.* **5**, 1083–1087 (2020).

Acknowledgements

Y.A.W. thanks the funding from New Frontiers Research Fund-Transformation (NFRFT-2022-00197), the Natural Sciences and Engineering Research Council of Canada (NSERC) (RGPIN-2020-05903, GECR-2020-00476), Tang Family Chair in New Energy Materials and Sustainability, Canadian Foundation for Innovation John R. Evans Leaders Fund (#41779), and Ontario Research Fund for Small Infrastructure (#41779). Z.T. acknowledges the funding from the NSERC collaborative research and treating experience program (CREATE) and GCI Ventures Capital, Toronto. This research used the resources of the Canadian Light Source and its funding partners. These works for in situ hard XAS, in situ FTIR, were performed at HXMA, Far-Infrared beamlines of the Canadian Light Source (CLS), a national research facility of the University of Saskatchewan, which is supported by the Canada Foundation for Innovation (CFI), the Natural Sciences and Engineering Research Council (NSERC), the National Research Council (NRC), and the Canadian Institutes of Health Research (CIHR), and the Government of Saskatchewan. Scanning Transmission Electron microscopy was performed at the Canadian Center for Electron Microscopy (also supported by NSERC and other government agencies). C.V.S. acknowledges the support of the Natural Sciences & Engineering Research Council of Canada (NSERC), University of Toronto. D.A. was supported by funding from the Canada First Research Excellence Fund (CFREF).

Author contributions

Y.A.W. conceived and supervised the project. Z.T. co-supervised the project. L.W. carried out the catalyst's synthesis, characterization, and performance test. L.W., X.W., M.H., and Z.L.C. carried out the XAFS measurements and data fitting. H.F. and R.S. assisted in the Raman test. D.A. helped with EPR measurements. N.C. provided advice for the XAFS measurements. B. B. guided the ATR FT-IR test. Y.X. and L.H. helped with material characterizations. L.W., Z.W.C., C.V.S., Z.T., and Y.A.W. wrote the paper. All authors made comments and revised the paper.

Competing interests

The authors declare no competing interests.

Additional information

Supplementary information The online version contains supplementary material available at https://doi.org/10.1038/s41467-024-52004-2.

Correspondence and requests for materials should be addressed to Chandra Veer Singh, Zhongchao Tan or Yimin A. Wu.

Peer review information *Nature Communications* thanks the anonymous, reviewer(s) for their contribution to the peer review of this work. A peer review file is available.